



## Pore-scale investigation of reactive transfer process in a deep eutectic solvent (DES) electrolyte-based vanadium-iron redox flow battery

Qiang Ma <sup>a, b</sup>, Lijuan Zhao <sup>c</sup>, Juncai Xu <sup>c</sup>, Huaneng Su <sup>a</sup>, Weiqi Zhang <sup>a</sup>, Weiwei Yang <sup>d</sup>, Qian Xu <sup>a,\*</sup>

<sup>a</sup> Institute for Energy Research, Key Laboratory of Zhenjiang, Jiangsu University, Zhenjiang, 212013, PR China

<sup>b</sup> Jiangsu Province Engineering Laboratory of High Efficient Energy Storage Technology and Equipments, China University of Mining and Technology, Xuzhou, 221116, PR China

<sup>c</sup> School of Energy and Power Engineering, Jiangsu University, Zhenjiang, 212013, PR China

<sup>d</sup> School of Energy and Power Engineering, Xi'an Jiaotong University, Xi'an, 710049, PR China



### ARTICLE INFO

#### Article history:

Received 26 October 2019

Received in revised form

19 April 2020

Accepted 10 May 2020

Available online 28 May 2020

#### Keywords:

Lattice Boltzmann method

Pore-scale

Cyclic voltammetry experiment

Deep eutectic solvents

Redox flow batteries

### ABSTRACT

In order to promote the applicability of redox flow batteries (RFBs), the deep eutectic solvents (DESs) have been proposed as a better choice for non-aqueous electrolyte of RFBs. The reactive transfer process within the RFB plays a key role in determining the cell performance. In this work, cyclic voltammetry experiment is conducted to obtain the reactive transfer property parameters of iron and vanadium ions in ethaline DES electrolyte. Then, a lattice Boltzmann method (LBM) model is utilized to reveal the reactive transfer mechanism of vanadium-iron RFB with DES electrolyte at the pore-scale. The numerical results present the influences of porous electrode morphology and DES electrolyte transfer properties on the performance of vanadium-iron RFB during galvanostatic discharging. This work suggests that the porous electrodes with the lower porosity and smaller fibre diameter lead to a more sufficient depletion time of reactant in DES electrolyte under the galvanostatic discharging and a given pumping power condition. Meanwhile, the larger fibre diameter yields the more widespread pore size distribution, resulting in the more apparent non-uniformity of local current density into the porous electrode. In addition, the results show the similar state of charge(SOC) in the cathode and anode under the same flow condition. By contrast, the absolute value of overpotential in the anode is significantly higher than that in the cathode. Furthermore, the reactive transfer process of this DES electrolyte-based vanadium-iron RFB is compared to all vanadium RFB with aqueous electrolyte under the galvanostatic discharging.

© 2020 Elsevier Ltd. All rights reserved.

## 1. Introduction

In recent years, redox flow batteries (RFBs), which have an unique feature of decoupled power and energy components, stand out as a promising grid-scale energy storage technology to facilitate the utilization of intermittent renewable energy sources, such as solar, wave, and wind energies [1]. Although existing RFB systems with aqueous electrolytes have been investigated widely [2,3], the energy density is still limited by lower solubility, stability of redox species in aqueous electrolytes and a narrow temperature window of RFBs [4,5]. Fortunately, deep eutectic solvents (DESs), as prospective concept in RFBs, have emerged for achieving RFBs of high

energy density [6]. DESs are room temperature liquid materials formed by the combination of an organic halide salt and a hydrogen bond donor with a stoichiometric ratio [7]. Nowadays, DESs are becoming the candidates of ionic liquids due to their potential merits including the lower price, easy to prepare, and chemical inertness with water [8]. Moreover, compared with the conventional aqueous electrolytes, DES electrolytes can offer higher electrochemical stability, wider potential window and larger solubility of redox species, anticipating to show superior performance in RFB systems [9].

In 2013, Lloyd et al. [10] proposed an all copper hybrid RFB, in which a DES consisting of choline chloride and ethylene glycol as electrolyte was used to dissolve copper ions. Nevertheless, this DES electrolyte-based RFB presents a low operation efficiency due to the limitation of poor transfer properties. Subsequently, Lloyd et al. [11] studied the characterization of Fe(II)/Fe(III) redox reaction in DES

\* Corresponding author.

E-mail address: [xuqian@ujs.edu.cn](mailto:xuqian@ujs.edu.cn) (Q. Xu).

electrolyte, and proposed a Fe-Zn RFB with an energy efficiency of 78% at the current density of  $5 \text{ A m}^{-2}$ . Furthermore, Xu et al. [12,13] characterized the electrochemical and transfer properties of the Fe(II)/Fe(III) and V(II)/V(III) redox couples in a reline DES electrolyte, and indicated a promising application of these redox couples in RFB systems. Then, Xu et al. [14] developed a DES electrolyte-based vanadium-iron RFB and studied the major factors that affect the efficiency of the RFB. Their experimental results show that the increased operating temperature will contribute to reducing the ohmic and pumping loss, thus resulting in an elevated energy efficiency of vanadium-iron RFB accordingly. Due to the performance of this RFB is dominated by the transfer properties of DES electrolytes [13,15], the great efforts are still needed to understand the mechanisms of electrolyte flow, mass and charge transfer processes coupling with the electrochemical reaction in the porous electrodes, thereby improving the usability of RFBs using DES electrolytes.

During the operation of RFBs, the reactive transfer process plays a key role in determining the performance of RFB, and which is governed by the electrolyte transfer conditions and morphological features of the porous electrodes [16]. As opposed to the expensive and challenging experimental study, numerical simulation provides an effective mean for understanding the complex transfer processes in the porous electrodes. Over the past decades, a series of macroscopic continuum models have been established to study the operational factors, such as electrolyte flow rate, electrochemical kinetics and electrode porosity, that affect the performance of all vanadium RFB (VRFB) with aqueous electrolytes at representative elementary volume (REV) scale [17–19]. In these REV scale models, the volumetric averaging conservation equations are employed based on the assumption of homogeneous porous component with electrolyte transfer properties, and ignore the description of structure details in the porous electrodes [20,21]. Hence, the macroscopic REV models may not be suitable to investigate the combined relation between the macroscopic reactive transfer properties and the microscopic pore structure characteristics of porous electrodes directly. On the contrary, the pore-scale simulation will be an applicable and effective approach in the study of the complex transfer processes in porous medium with the realistic structures [22–24]. For the pore-scale model of the stochastic porous media, one of the difficulties lies in the treatment of irregular boundaries in pore structures. However, as result of the prominent advantages including the convenient implementation in complex boundary conditions and the high level of parallel computation [25–27], lattice Boltzmann method (LBM) was proved to be an accurate and efficient method for the numerical simulation at the pore-scale [28], and has been applied to understand the reactive transfer process in the pore structures of electrodes [29–31].

In 2012, Qiu et al. [32,33] utilized LBM to simulate the aqueous electrolyte flow in a three-dimensional porous electrode of VRFB regenerated by the X-ray computed tomography technology. Combining with finite volume method (FVM), they proposed a LBM-FVM numerical model to solve the coupled reactive transfer and predict the performance of VRFB under different operating conditions. Then, Chen et al. [34] employed LBM to study the multiphase flow and reactive transfer behaviors in the porous electrodes of VRFB. In this numerical model, based on the assumption of uniform overpotential at the interface of electrodes, the mass transfer of vanadium ions and the flow of aqueous electrolyte were simulated using the multiple-relaxation-time (MRT) LBM coupling with a pore-scale electrochemical reaction model. Similarly, Zhang et al. [35] adopted three-dimensional LBM to model the coupled transport behaviors in the aqueous electrolyte-based VRFB at the pore-scale. In their study, a concise LB scheme

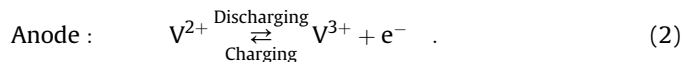
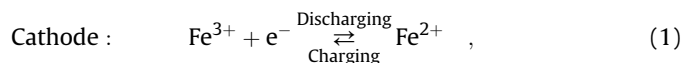
was applied to simulate the charge transfer process to obtain the distributions of current density and overpotential in the carbon paper electrode of VRFB. Recently, Zhang et al. [36] conducted a 3D LB simulation of non-aqueous RFB on the electrodes with different microstructure. The numerical results show that the electrode microstructure plays an important role in the performance of RFB. As a conclusion, LBM was demonstrated as a powerful numerical simulation tool for understanding the coupled reactive transfer process in the porous electrodes, thereby optimizing the operating performance of RFB.

In our previous work, we developed a three-dimensional MRT-LBM to solve the complex transfer behaviors in the porous electrode of all copper redox flow battery using DES electrolyte, and the effects of operating temperature on the operation of cathode in this RFB were studied using this model [37]. Nevertheless, the reactive transfer process of non-aqueous RFB influenced by the morphology of the porous electrodes (e.g. fibre diameter, connectedness, pore size distribution and anisotropy) is also required to further investigate by LB method. Moreover, a pore-scale analysis for the performance of vanadium-iron RFB using DES electrolyte has not been reported in the present literature. Based on the specific transport and reactive characteristics of vanadium-iron RFB, the pore-scale simulation of reactive transfer process in the cathode and anode will contribute to optimizing the performance of this promising RFB system in future.

In this paper, firstly, in order to determine the key property parameters of iron and vanadium ions in the ethaline DES electrolyte required in the simulation study, cyclic voltammetry experiment is conducted in a three-electrode system. Then, the pore-scale LBM model is established for this operation simulation of RFB using DES electrolyte, and the implementation details of this numerical model are introduced. Meanwhile, the reconstructed carbon paper electrodes with the different morphological features are generated utilizing a random reproducing algorithm. Finally, a pore-scale investigation is performed to analyze the reactive transfer process in the reconstructed electrodes of vanadium-iron RFB using DES electrolyte during galvanostatic discharging. The effects of morphology of porous electrode and transfer properties of ethaline DES electrolyte on the performance of vanadium-iron RFB (including cathode and anode) are elaborated and compared with VRFB using aqueous electrolyte in numerical results section.

## 2. Experimentally determined reactive and transport parameters

During the discharging and charging cycles of vanadium-iron RFB, the following reactions take place in the positive porous electrode (i.e., cathode) and the negative porous electrode (i.e., anode) [38]:



For sake of simplicity,  $\text{Fe}^{2+}$  is marked as Fe(II),  $\text{Fe}^{3+}$  is marked as Fe(III),  $\text{V}^{2+}$  is marked as V(II),  $\text{V}^{3+}$  is marked as V(III) respectively.

As mentioned in the above introduction, the coupled transfer process is a key factor in affecting the electrochemical reaction of RFB. However, due to the scarce experimental data about the reactive and transfer property parameters of vanadium-iron RFB with non-aqueous electrolyte of ethaline system, cyclic voltammetry experiment measurements were carried out to determine

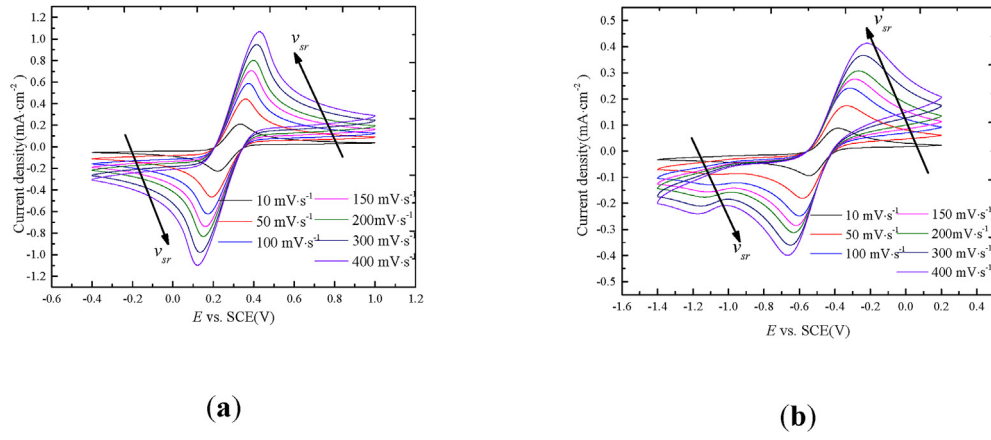


**Fig. 1.** Cyclic voltammetry curves of positive and negative side electrolyte. (a) Positive side electrolyte; (b) Negative side electrolyte.

the electrochemical and transfer properties of the iron and vanadium ions in the ethaline DES electrolyte.

DES electrolyte was prepared as follows: choline chloride was blended in ethylene glycol with a molar ratio of 1–2, and then stirred at 373 K, resulting in a colorless liquid solution. The solution was sealed in a jar until cooling down to room temperature and the obtained solution was denoted as DES electrolyte. After that, the positive side electrolyte(i.e, catholyte) [39] was prepared by dissolving a certain amount of anhydrous  $\text{FeCl}_3$  (Fluka® 97%) in the DES electrolyte and the concentration of  $\text{FeCl}_3$  was controlled at 0.1 mol L<sup>-1</sup>. The negative side electrolyte (i.e, anolyte) [39] was obtained in the same manner using  $\text{VCl}_3$  (Vokai® 97%) as the redox species.

The cyclic voltammetry was conducted in a three-electrode one-component electrochemical cell with a CHI 660E electrochemical workstation at room temperature [40]. A Pt wire and a saturated calomel electrode (SCE) were used as counter electrode and reference electrode, respectively. A glassy carbon electrode (GCE) with a diameter of 5 mm was used as working electrode.

Fig. 1 shows the cyclic voltammetry curves of catholyte and anolyte with different scan rates( $v_{sr}$ ). It can be found that the redox peak currents increase with the rising scan rates. In order to analyze the effect of scan rate on the electrochemical behavior, the relationship between peak current and square root of scan rate is plotted in Fig. 2, which appears a typical linear correlation. Actually, based on Randles-Sevcik model, the oxidation or reduction peak current  $i_p$  in reversible electrochemical reaction can be calculated as [12]:

$$i_p = 2.69 \times 10^5 An^{1.5} CD_{re,O/R}^{0.5} v_{sr}^{0.5} \quad (3)$$

On the right side of the above equation,  $A$  denotes the area of the reaction electrode,  $n$  denotes the number of electrons transferred in the reaction.  $C$  denotes the bulk concentration of the redox species,  $D_{re,O/R}$  denotes the diffusivities of oxidized or reduced species in reversible reaction. It is obvious that the diffusivity can be predicted through the linear fitting method from the experimental data.

On the other hand, for an irreversible reaction, the relationship between peak current and diffusivities of oxidized or reduced species ( $D_{irre,O/R}$ ) in irreversible reaction can be written as [12]:

$$i_p = 2.99 \times 10^5 \alpha^{0.5} CD_{irre,O/R}^{0.5} v_{sr}^{0.5} \quad (4)$$

where the charge transfer coefficient is  $\alpha$ .

In the actual operating process of RFB, the electrochemical reaction is often in between reversible and complete irreversible reaction which can be considered as quasi-reversible reaction. In this system, the peak current  $i_p$  is given by the modified Randles-Sevcik equation [41]:

$$i_p = i_p(\text{rev})K(\lambda, \alpha) \quad (5)$$

where the  $i_p$  (rev) means the peak current of reversible reaction determined by Eq. (3), and  $K(\lambda, \alpha)$  is a characteristic parameter that depends on the charge transfer coefficient  $\alpha$  and another dimensionless parameter  $\lambda$ .

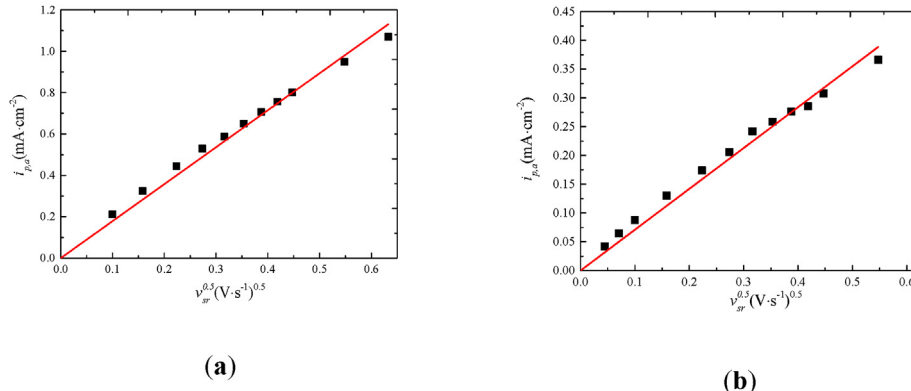


**Fig. 2.** Peak current density at different square root of scan rates. (a) Positive side electrolyte; (b) Negative side electrolyte.

Moreover, for the quasi-reversible system, the relationship between peak potential and scan rate can be expressed as:

$$E_p = E_0 - \frac{RT}{\alpha nF} [0.780 - \ln k_0 + \ln(\frac{D\alpha nFv_{sr}}{RT})^{0.5}] \quad (6)$$

In above equation,  $E_p$  denotes the potential corresponding to the peak current, which can be obtained from the cyclic voltammetry curves,  $E_0$  denotes the formal potential of electrochemical reaction, which is obtained using the average value of oxidation peak potential and reduction peak potential.  $R$  is the universal gas constant,  $T$  is the temperature,  $F$  is Faraday's constant,  $n$  is the transfer electron number. The above equation also can be written as a linear equation to describe the relationship between  $E_p - E_0$  and  $\ln(v_{sr})$ . Hence, the slope and intercept of this linear equation are expressed as:

$$\text{Slope} = -\frac{RT}{2\alpha nF} \quad (7a)$$

$$\text{Intercept} = -\frac{RT}{\alpha nF} [0.780 - \ln k_0 + \ln(\frac{D\alpha nF}{RT})^{0.5}] \quad (7b)$$

Based on the cyclic voltammetry data, the slope and intercept can be obtained by the linear fitting method as shown in Fig. 3. It is obvious that the charge transfer coefficient  $\alpha$  can be estimated by Eq. (7a) as listed in Table 1. Then, the diffusivities in irreversible reaction are predicted based on the known charge transfer coefficient and Eq. (4).

In this work, based on our previous experimental work [12,13], the average diffusivities of redox species in this simulation is estimated using the arithmetic mean value of  $D_{re}$  and  $D_{irre}$ , as listed in Table 1. In order to confirm the reliability of estimated diffusivities, the effective ranges of diffusivities in quasi-reversible system are calculated by Eq. (5), and a dimensionless parameter  $\psi$  ( $\psi = \Lambda\pi^{-1/2}$ ) is introduced to determine the  $K(\Lambda, \alpha)$  of Eq. (5). The variation of  $\psi$  with the experimental peak separation  $\Delta E$  can be obtained from Nicholson method [42]. Thus, using the known  $\psi$  and  $\alpha$ , the range of parameter  $K(\Lambda, \alpha)$  can be estimated based on the literature [41]. Substituting the  $K(\Lambda, \alpha)$  into Eq. (5), the diffusivities  $D_{O/R}$  of iron ions are determined within the range from  $1.12 \times 10^{-11} \text{ m}^2 \text{ s}^{-1}$  to  $1.43 \times 10^{-11} \text{ m}^2 \text{ s}^{-1}$ , and the diffusivities  $D_{O/R}$  of vanadium ions are determined within the range from  $1.78 \times 10^{-12} \text{ m}^2 \text{ s}^{-1}$  to  $2.35 \times 10^{-12} \text{ m}^2 \text{ s}^{-1}$ . It can be found that the selected diffusivities in Table 1 are expected in the above ranges. Furthermore, inspired by the literature [43], we also used another calculation method to estimate the parameter  $K(\Lambda, \alpha)$ , and determine the range of diffusivities in quasi-reversible system(see appendix A). It can be seen

**Table 1**

Transfer properties of the iron and vanadium ions in the ethaline electrolyte.

Quantity	Value
Diffusivity of Fe, $D_{Fe(II)}$ , $D_{Fe(III)}$	$1.37 \times 10^{-11} \text{ m}^2 \text{ s}^{-1}$ , $1.21 \times 10^{-11} \text{ m}^2 \text{ s}^{-1}$
Diffusivity of V, $D_{V(II)}$ , $D_{V(III)}$	$1.99 \times 10^{-12} \text{ m}^2 \text{ s}^{-1}$ , $1.92 \times 10^{-12} \text{ m}^2 \text{ s}^{-1}$
Transfer coefficient of Fe, $\alpha_1$	0.49
Transfer coefficient of V, $\alpha_2$	0.45
Reaction constant of Fe, $k_{01}$	$1.75 \times 10^{-6} \text{ m s}^{-1}$
Reaction constant of V, $k_{02}$	$2.30 \times 10^{-7} \text{ m s}^{-1}$

that the diffusivities of redox species in Table 1 also meet the effective ranges from this calculation method.

In addition, using the known diffusivity and transfer coefficient, the reaction constant  $k_0$  of iron and vanadium ions in the ethaline electrolyte are estimated by Eq. (7b), as listed in Table 1. On the other hand, Nicholson [42] introduced that the potential peak separation is largely independent of the transfer coefficient when it lies within the range of 0.3–0.7, and the dimensionless number  $\psi$  can be defined as:

$$\psi = \frac{(D_O/D_R)^{\alpha/2} k_0}{(\pi D_O^{nF} v_{sr})^{0.5}} \quad (8)$$

Based on the dimensionless number  $\psi$  predicted in the applicable scope of Nicholson method, and the range of reaction constant can be estimated by Eq. (8). Using the results of this cyclic voltammetry data, the reaction constants of iron and vanadium ions should be in that ranges of  $1.43 \times 10^{-6} \text{ m s}^{-1}$ – $2.43 \times 10^{-6} \text{ m s}^{-1}$  and  $2.12 \times 10^{-7} \text{ m s}^{-1}$ – $3.15 \times 10^{-7} \text{ m s}^{-1}$  respectively. It can be found that the ranges accord with the prediction as listed in Table 1.

### 3. Numerical method and details

#### 3.1. Numerical model

The electrolyte flow, the transport of ions and electrons in the porous electrode and the electrochemical reaction as the fundamental physical processes are considered in this work. In order to simplify this mathematical model, several assumptions are proposed as follows [32]: (1) DES electrolyte is an incompressible Newtonian fluid with invariable viscosity; (2) the no-slip boundary condition is implemented at the fibre surface of porous electrode; (3) the operation of RFB is an isothermal process under stable room temperature (298K); (4) the influence of ionic species on the flow field is not considered. The macroscopic governing equations are

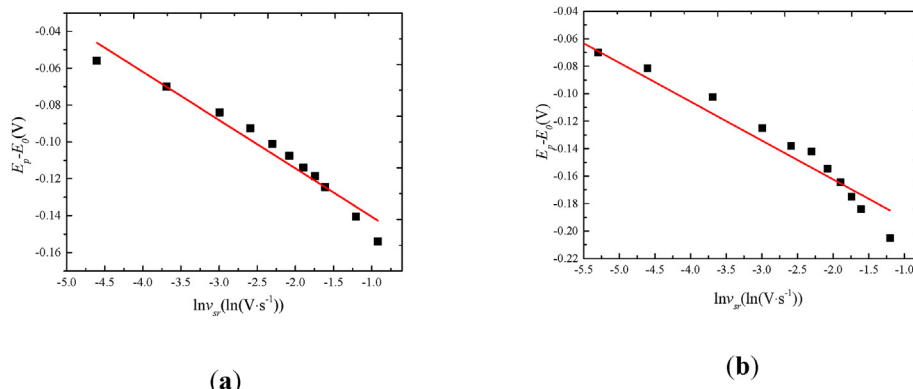


**Fig. 3.** Relationship between peak potentials and scan rates. (a) Positive side electrolyte; (b) Negative side electrolyte.

**Table 2**  
Macroscopic governing equations.

Description	Conservation equations	Annotation
Flow of electrolyte	$\nabla \cdot \mathbf{u} = 0, \frac{\partial \mathbf{u}}{\partial t} + (\mathbf{u} \cdot \nabla)(\mathbf{u}) = -\frac{1}{\rho_0} \nabla p + \nu \nabla^2 \mathbf{u}$	$u$ is the flow velocity and $\rho_0$ is the density of DES electrolyte respectively, $p$ and $\nu$ denote the pressure and viscosity of DES electrolyte respectively.
Transfer of ions	$\frac{\partial C_i}{\partial t} + \nabla(\mathbf{u}C_i) = D_i \nabla^2 C_i + \nabla \cdot \left[ \frac{z_i C_i D_i}{RT} \nabla \phi \right]$	$C_i, D_i$ and $z_i$ are the ion concentration, diffusivity and charge of species $i$ respectively.
Transfer of electrons	Electrode: $\nabla \cdot (\kappa_s \nabla \phi_s) = 0$ , Electrolyte: $\nabla \cdot [(\kappa_e \nabla \phi_e) + F \sum z_i D_i \nabla C_i] = 0$	$\phi$ is the electrical potential. $\kappa_s$ and $\kappa_e$ are the electrical conductivity of the fibre electrode and electrolyte respectively.

listed in [Table 2](#). These equations are solved using a pore-scale LBM model, and explained in detail in our previous work [\[37\]](#).

For the sake of simplicity, the migration term on the right hand side of ions transfer equation can be neglected based on the research results from previous studies [\[34,35\]](#). The electrochemical reaction at the carbon electrode fibre surface has been described as Eq. [\(1\)](#) and Eq. [\(2\)](#). The relationship between the mass flux  $J_i$  caused by electrochemical reaction and the overpotential at the electrode interface during discharging can be calculated using Butler–Volmer equation:

$$\text{Cathode : } J_{1II} = -J_{1III} = k_{01}(C_{1II})^{\alpha_1}(C_{1III})^{\alpha_1} [\exp(\frac{\alpha_1 F \eta_1}{RT}) - \exp(-\frac{\alpha_1 F \eta_1}{RT})] \quad (9a)$$

$$\text{Anode : } -J_{2II} = J_{2III} = k_{02}(C_{2II})^{\alpha_2}(C_{2III})^{\alpha_2} [\exp(\frac{\alpha_2 F \eta_2}{RT}) - \exp(-\frac{\alpha_2 F \eta_2}{RT})] \quad (9b)$$

where the overpotential  $\eta_1$  and  $\eta_2$  are obtained using:

$$\eta_1 = \phi_s - \phi_e - E_1 \quad (10a)$$

$$\eta_2 = \phi_s - \phi_e - E_2 \quad (10b)$$

and the effective voltages  $E_1, E_2$  on respective electrodes can be given by:

$$E_1 = E_{01} + \frac{RT}{F} \ln(\frac{C_{1III}}{C_{1II}}) \quad (11a)$$

$$E_2 = E_{02} + \frac{RT}{F} \ln(\frac{C_{2III}}{C_{2II}}) \quad (11b)$$

It is important to clarify that the species concentration at the node near carbon fibres is considered as the species concentration at the active surface approximately [\[32\]](#). Therefore, the concentration overpotential is not taken into account in this present work. In addition, the state of charges (SOCs) of the catholyte and anolyte are defined as:

$$SOC = \frac{C_{1III}}{C_{10}} = \frac{C_{2II}}{C_{20}} \quad (12)$$

where  $C_{10}, C_{20}$  denote the total active ion concentration in the catholyte and anolyte, respectively.

Furthermore, a verification case of VRFB is provided in appendix B. Although the differences of reactive and transport parameters exist between the vanadium-iron RFB and VRFB, the pore-scale reactive transport behaviors of two RFB systems can be described using the same mathematical model with different physical parameters. Thereby, due to the lack of reported data of vanadium-iron RFB from other literature, the benchmark case of VRFB is performed to validate the LB model can be used as a solver of pore-scale reactive transport process of RFBs.

### 3.2. Numerical details

The schematic diagram of pore-scale simulation for vanadium-iron RFB is shown in [Fig. 4](#). The computational domain includes a cathode and an anode, which are divided by the ion-exchange membrane. In this work, the mass flux at electrolyte/membrane interface is set as zero for all ionic species. As a theoretical research, the effect of ion crossover on the performance of RFB is not

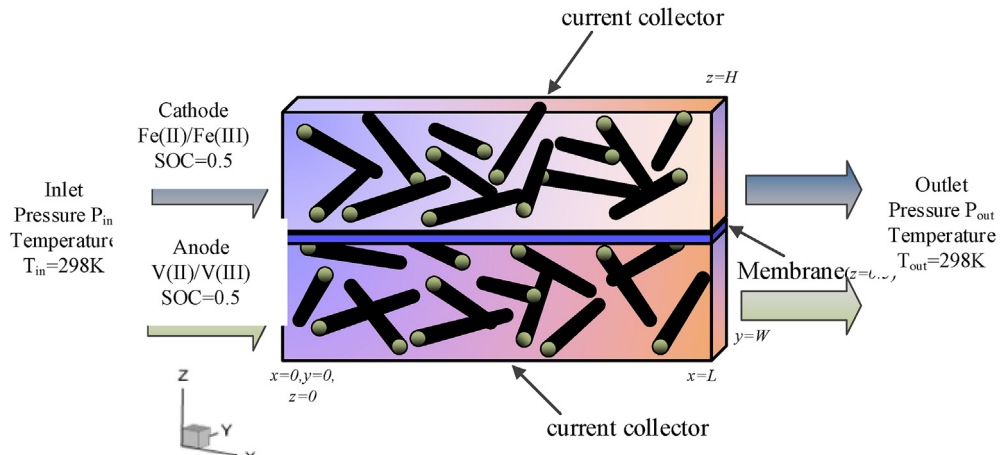


**Fig. 4.** Schematic diagram of pore-scale simulation for vanadium-iron RFB.

**Table 3**  
Boundary conditions for individual.

Boundary location	Boundary conditions
$x = 0$	$P_{x=0} = P_{in}$ , $C_2 = SOC \cdot C_0$ , $C_1 = (1-SOC) \cdot C_0$ , $\kappa_s \frac{\partial \phi_s}{\partial x} = 0$ , $\kappa_e \frac{\partial \phi_e}{\partial x} = 0$
$x = L$	$P_{x=L} = P_{out}$ , $D_i \frac{\partial C_i}{\partial x} = 0$ , $\kappa_s \frac{\partial \phi_s}{\partial x} = 0$ , $\kappa_e \frac{\partial \phi_e}{\partial x} = 0$ $\frac{\partial u_x}{\partial x} = 0$ , $\frac{\partial C_i}{\partial x} = 0$ , $\frac{\partial u_x}{\partial x} = 0$ , $\frac{\partial C_i}{\partial x} = \frac{\partial u_x}{\partial x} = 0$ , $\frac{\partial C_i}{\partial x} = 0$ , $\frac{\partial u_x}{\partial x} = 0$ , $\frac{\partial C_i}{\partial x} = 0$
$z = 0.5$ (membrane)	$u_{z=0.5} = 0$ , $D_i \frac{\partial C_i}{\partial z} = 0$ , $\kappa_s \frac{\partial \phi_s}{\partial z} = 0$ , $\kappa_e \frac{\partial \phi_e}{\partial z} = \pm I_{ext}$
$z = 0, z = H$ (current collector)	$u_{z=0,H} = 0$ , $D_i \frac{\partial C_i}{\partial z} = 0$ , $\kappa_s \frac{\partial \phi_s}{\partial z} = \pm I_{ext}$ , $\kappa_e \frac{\partial \phi_e}{\partial z} = 0$
$y = 0, y = W$	$\frac{\partial u}{\partial y} = 0$ , $D_i \frac{\partial C_i}{\partial y} = 0$ , $\kappa_s \frac{\partial \phi_s}{\partial y} = 0$ , $\kappa_e \frac{\partial \phi_e}{\partial y} = 0$

considered in the present work. In order to consider the chloride ions transport across the membrane, the bulk generation and depletion of chloride ions in the catholyte and anolyte are estimated based on electroneutrality, which is a simplified method proposed by Qiu et al. [32]. Therefore, the cathode and anode can be simulated independently.

Moreover, a constant external current is applied on the current collectors at  $z = 0$  and  $z = H$  to model the galvanostatic discharging process of RFB. It's worth noting that the electrolyte flowing is derived by the pumping in the real RFB system. As a theoretical assumption, a given pressure difference along x-axis is employed to indicate the required pumping power imposing on the different porous electrodes. The boundary conditions in detail are presented in Table 3.

The electrochemical reaction behaviors are coupled into the pore-scale transport model of LBM using the implementation method of reactive boundary condition. Considering the electrochemical reaction during discharging, Neumann boundary is used at the interface of carbon fibres based on the above kinetic model:

$$-D_1 \frac{\partial C_1}{\partial n} = D_2 \frac{\partial C_2}{\partial n} = k_0 (C_1)^{\varphi} (C_2)^{\varphi} [\exp(\frac{\varphi F \eta}{RT}) - \exp(-\frac{\varphi F \eta}{RT})] \quad (13)$$

In this work, the unknown concentration distribution  $g \alpha i$  is given by the boundary treatment scheme from literature [44]. In addition, the boundary scheme for electric potential at the interface of carbon fibre is obtained using the local current density [37]:

$$\frac{\partial \phi}{\partial n} = \pm I \quad (14)$$

The nondimensional treatment is a necessary step in the LBM simulation. In this work, several dimensionless numbers are proposed to associate lattice unit with the real physical unit, including Reynolds number  $Re$ , dimensionless time  $Fo$ , dimensionless pressure  $Be$ , dimensionless reaction constant  $Da$ , dimensionless concentration  $C^*$ , dimensionless mass flux  $J^*$ , which are defined as follows:

$$\begin{aligned} Re &= \frac{U_0 L}{v}, \quad Fo = \frac{D_1 t}{L^2}, \quad Be = \frac{\Delta P L^2}{\rho_0 v^2}, \quad Da = \frac{k_0 L}{D_1}, \\ C^* &= \frac{C}{C_0}, \quad J^* = \frac{J_{mass} L}{C_0 \cdot D_1} \end{aligned} \quad (15)$$

where  $L$  means the characteristic length,  $U_0$  means the

characteristic velocity of the porous electrode, and  $t$  means the computation time for the coupled transfer processes.

### 3.3. Random reproducing method of 3D porous electrode

Many carbon-based materials have been applied as porous electrodes in real RFBs, including graphite felt, carbon felt, and carbon paper. Due to the different physiochemical properties and cost [45–48], the difference of electrode materials has great effect on the performance of RFBs. At the pore-scale, the morphology of different porous electrodes (e.g., graphite felt and carbon paper) also plays a key role in the operation of RFBs [36]. This paper mainly focuses on the reactive transfer process of non-aqueous RFBs in the carbon paper electrodes with the different morphological features. Based on the acquired statistical information of porous carbon paper electrodes such as porosity and fibre diameter, three dimensional microporous structures of carbon paper are reproduced using a random generation algorithm [49,50], the reproducing procedure [34] of which is elaborated in Fig. 5. In addition, the details of this algorithm and the morphology of generated porous electrodes are illustrated in appendix C.

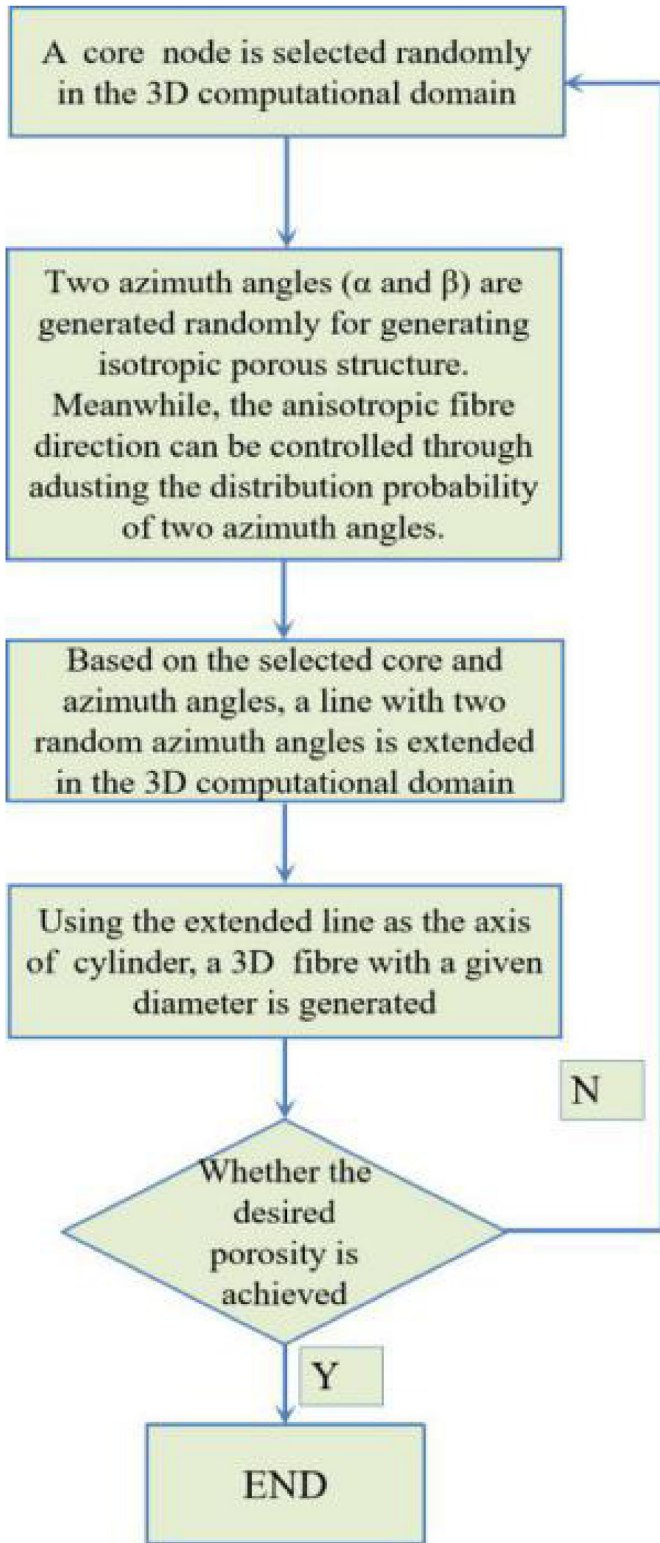
Based on the reproducing process, the main geometrical parameters of porous electrodes in this simulation are listed in Table 4. Owing to the limitation of computing resource, the whole morphology of a real carbon paper is difficult to reconstruct in this pore-scale simulation. The reproduced porous structure as shown in Fig.C.1 can be viewed as the local structure of a thin carbon paper with the thickness of 140  $\mu\text{m}$ . Moreover, a larger length (320  $\mu\text{m}$ ) is chosen along x-axis due to the variation of species concentration mainly appears in this direction of electrolyte flow.

## 4. Numerical results and discussions

Based on the LBM model and random reproducing of porous electrodes introduced in above section, the reactive transfer process of vanadium-iron RFB with ethaline DES electrolyte is simulated at the pore-scale. The key transfer properties of the iron and vanadium ions have been obtained using the cyclic voltammetry experiment as shown in Table 1. In addition, the other related model parameters of this work are listed in Table 5.

### 4.1. Effect of morphological features of isotropic porous electrodes

The effects of morphological features of porous electrodes on

**Fig. 5.** Reproducing procedure of porous electrode.

the performance of vanadium-iron RFB during galvanostatic discharging are investigated at the same dimensionless differential pressure, which means the equal required pumping power per unit time in the operating of RFB. For the isotropic porous electrodes with the different porosity and fibre diameter, the detailed concentration distributions of Fe(III) along x-axis with the different

**Table 4**  
Parameters of reconstructed porous structure.

Quantity	Value
Length $L$	320 $\mu\text{m}$
Width $W$	140 $\mu\text{m}$
Height $H$	140 $\mu\text{m}$
Porosity $\epsilon$	0.83–0.93
Fibre fibre diameter $d_f$	6–14 $\mu\text{m}$
Grid resolution	2 $\mu\text{m}$ voxel $^{-1}$

**Table 5**  
Operating parameters of vanadium-iron RFB simulation.

Quantity	Value
Dimensionless differential pressure $B_e$	$0.153 \times 10^5$
Inlet SOC	0.5
External current density $I_{ext}$	400 A m $^{-2}$
Solid Electrical conductivity $\kappa_s$	1000 S m $^{-1}$
Viscosity of DES electrolyte, $\eta_v$	41 mPa s [51]
Universal gas constant, $R$	8.314 J mol $^{-1} \cdot \text{K}^{-1}$
Inlet concentration $C_0$	1000 mol m $^{-3}$
Initial chloridion concentration	6000 mol m $^{-3}$

porosity are illustrated in Fig. 6(a). The results show that Fe(III) ions have a higher depletion rate in the porous electrodes with the lower porosity. The reason is caused by the lower porosity leads to the larger flow resistance of DES electrolyte, which reduces the flow velocity of ethaline electrolyte at the same differential pressure and prolongs the reaction time of Fe(III) ions under the galvanostatic discharging condition [37].

Besides the effect of porosity, this work presents the concentration distributions of Fe(III) ions in the porous electrodes with the different fibre diameter, as shown in Fig. 6(b). For the porous electrodes with a porosity of 0.83, it is found that the average concentration of Fe(III) increases with the increasing fibre diameter. These results imply that the smaller fibre diameter causes the more sufficient reduction reaction of iron ions in the catholyte. The influences of fibre diameter on the transfer performance in fibre porous media have been investigated in previous literature [34,52]. These experimental and numerical studies pointed out that the larger diameter of carbon fibre will improve the permeability and effective diffusivity, due to the decreasing tortuosity of porous electrodes at a given porosity. To illustrate this point, the chord-length distribution  $l_C$  is introduced to straightforward reflect the tortuosity of porous electrodes. The chord-length distribution is a length distribution of straight lines along orthogonal directions in pores, and two endpoints of a line are located at the fluid-solid interface [53]. As a typical topography parameter of porous media, the chord-length distribution is used for assessing the connectedness of stochastic porous media [54]. It is obvious that the negative relationship between the mean chord-length and tortuosity. Fig. 7(a) shows the mean chord-length along x-axis direction increases with the increasing porosity and diameter of carbon fibre. For the porous electrodes with a porosity of 0.9, the mean chord-length rises 74% when the fibre diameter varies from 6  $\mu\text{m}$  to 14  $\mu\text{m}$ , which implies the decreasing tortuosity along flow direction reduces the seepage resistance in the porous electrodes. As a result, the flow velocity of ethaline electrolyte is improved in the porous electrodes of larger fibre diameter at the same differential pressure condition depicted in Fig. 7(b), and the depletion time of reactant is shortened to the increasing concentration of Fe(III) ions.

Accordingly, the average SOC of ethaline electrolyte in the cathode is showed in Fig. 7(c). Due to the influence of the morphological features of porous electrodes on the electrolyte flow

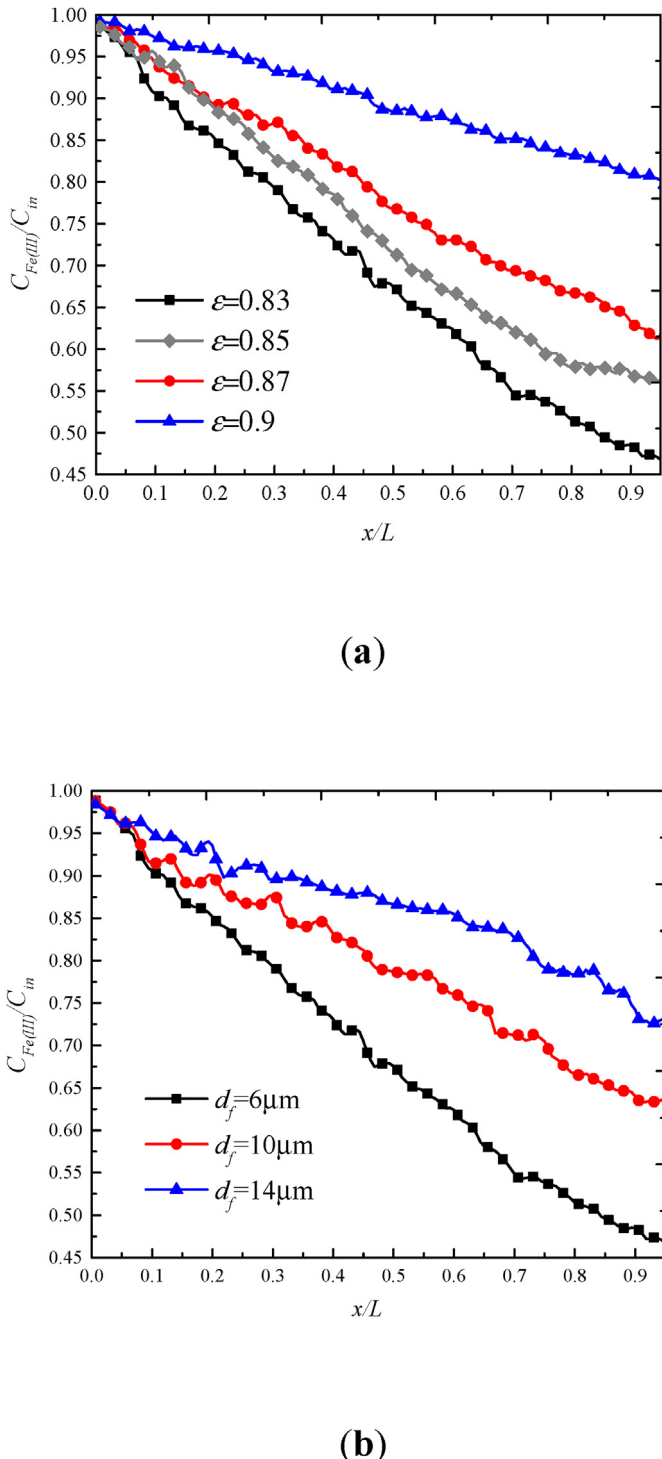


**Fig. 6.** Effect of electrode morphology on the concentration distributions of Fe(III) ions. (a) Concentration distributions with different porosity,  $d_f = 6 \mu\text{m}$ ; (b) Concentration distributions with different fibre diameters,  $\epsilon = 0.83$ .

as discussed above, a higher depletion time of electrochemical reactant is presented in the cathode with the lower porosity and smaller fibre diameter, which leads to the lower average SOC of ethaline electrolyte under the galvanostatic discharging and a given required pumping power condition. The reason is caused by the subdued effect of electrolyte flow on the operating of RFB at the larger  $Re$  number [33], the difference of Fe(III) concentration is

reduced in the porous electrodes with the higher porosity and larger fibre diameter.

On the other hand, the variation of porosity and fibre diameter will affect the specific surface area ( $S$ ) of carbon fibre in the porous electrodes. It is obvious that the dimensionless specific surface area decreases with the increasing porosity, and the porous electrodes with the higher carbon fibre diameter have a lower specific surface area. Because the interface of carbon fibre is the site where the electrochemical reaction takes place, the lower specific surface area will improve the average local transfer current density at the carbon fibres interface [37]. According to Butler-Volmer equation, the improving local transfer current density leads to the increase of absolute value of overpotential at the carbon fibres interface. Hence, the higher porosity and larger fibre diameter yield the increasing absolute value of overpotential as shown in Fig. 7(d), and which gives rise to the decline of discharging voltage and electrolyte utilization efficiency under the galvanostatic discharging.

In addition, although the local transfer current density decreases with the increasing specific surface area, the average value of product between local transfer current density and dimensionless specific surface area should be close to the external current density (i.e.,  $400\text{A/m}^2$ ) under the galvanostatic discharging, which is in agreement with the prediction of this simulation as shown in Fig. 8(a). However, it can be seen a visible difference in the standard deviation of local current density with the different fibre diameter depicted by the capped bars. This result implies the uniformity of local transfer current density reduces at a larger fibre diameter, and the reason can be explained by the effect of fibre diameter on the pore size distribution of porous electrodes. In our work, the pore size distribution of reconstructed porous electrodes can be calculated using the diameter density distribution of intercontacting spheres in pores. Based on the computation procedure of pore size distribution described by the literature [35], the pore size distribution of porous electrodes with different fibre diameter and a porosity of 0.9 are calculated and plotted in Fig. 8(b). It can be found that the reconstructed porous electrode of  $6 \mu\text{m}$  fibre diameter shows narrowly pore size distribution with a dominant peak around  $2 \mu\text{m}$ , and all pore sizes are under  $34 \mu\text{m}$ . In contrast, the porous electrodes with  $10$  and  $14 \mu\text{m}$  fibre diameter have the wider pore size distribution, especially the volume of mesoscopic pore in the range of  $15\text{--}40 \mu\text{m}$  is significantly higher than the porous electrode of  $6 \mu\text{m}$  fibre diameter. The widespread pore size distribution gives rise to the non-uniform flow distribution of DES electrolyte in the pores of electrode [36]. The variance of concentration distribution is extended in the electrodes with larger fibre diameter, thus resulting in the more apparent non-uniformity of local current density.

#### 4.2. Effect of anisotropy of porous electrodes

The above results are obtained from this simulation in the isotropic porous electrodes, and the effect of anisotropy of porous electrode on the reactive transfer process is investigated in this work. The three-dimensional anisotropic pore structures of porous electrodes with the porosity of 0.9 and fibre diameter of  $6 \mu\text{m}$  are reconstructed as shown in Fig. C.1(d) and (e), that are defined as in-plane structure and cross-plane structure respectively. Using the same operating parameters listed in Table 5, the comparison of  $Re$  number of electrolyte between the isotropic and anisotropic porous electrodes is shown in Fig. 9(a). The figure depicts that the electrolyte flow velocity in the in-plane porous electrode is slightly higher than the isotropic porous electrode with the porosity of 0.9 and fibre diameter of  $6 \mu\text{m}$ . On the contrary, the average flow velocity of ethaline electrolyte in the cross-plane porous electrode is lower than other pore structures. The outcome reveals the

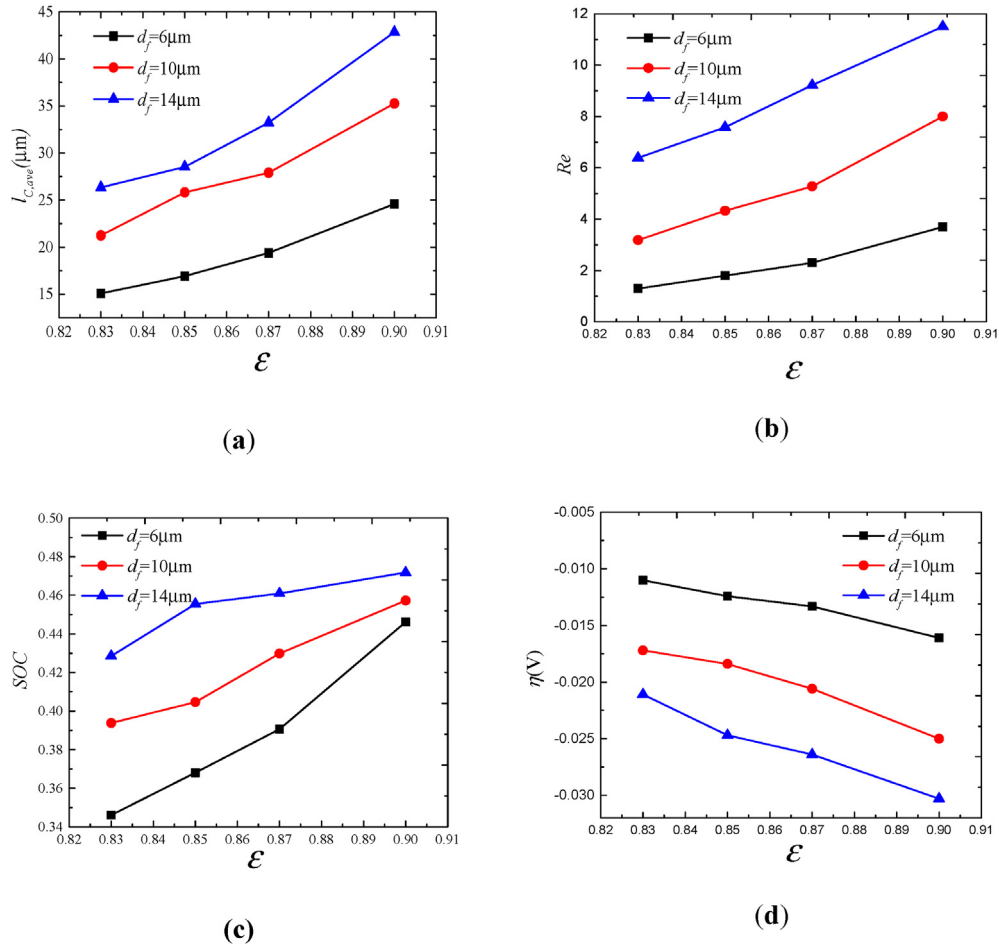


**Fig. 7.** Effect of electrode morphology on the performance of vanadium-iron RFB with DES electrolyte. **(a)** Mean chord-length of porous electrodes; **(b)** Re number of electrolyte in positive electrodes; **(c)** Average SOC of electrolyte in positive electrodes; **(d)** Overpotential of different positive porous electrodes.

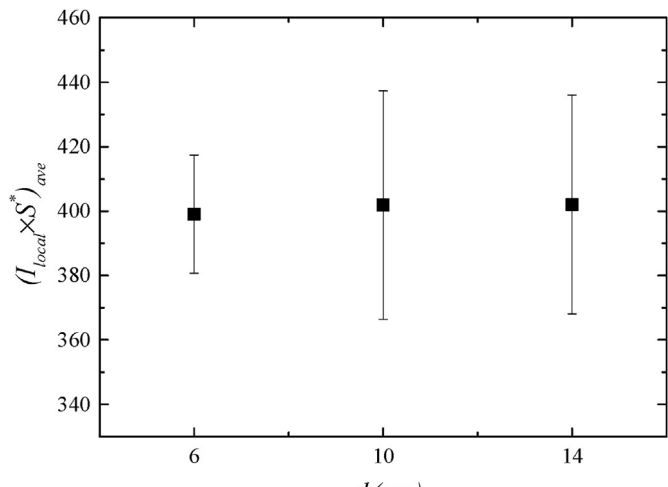
tortuosity of porous electrode is affected by the anisotropy of fibre pore structure, as shown in Fig. 9(b). It can be seen that the cross-plane porous electrode has a largest tortuosity due to the opposite relationship between the mean chord-length and the tortuosity. When the ethaline electrolyte flows along the cross-plane direction, the overlapping carbon fibres increase the tortuosity of electrolyte streamline, thereby reducing the permeability in the cross-plane porous electrode. As a result, the lower electrolyte flow leads to the more depletion of Fe(III) ions, which gives rise to the lower average SOC in the porous electrode as the electrolyte flowing along the cross-plane direction, as shown in Fig. 9(c). In addition, due to the same topological characteristics such as porosity and fibre diameter, the specific surface area of three porous structures are similar, finally inducing the close overpotential as shown in Fig. 9(d). The slight difference in this figure may be caused by the randomness of porous reproducing algorithm.

#### 4.3. Comparison between cathode and anode

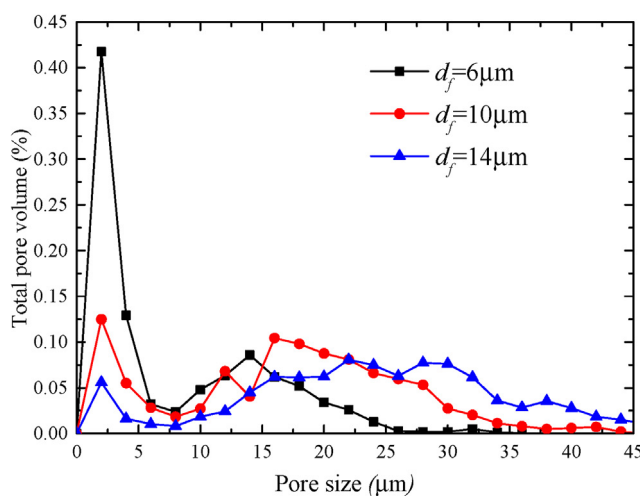
In this section, the comparative investigation of reactive transfer process in the cathode and anode is performed. In order to eliminate the effect of random pore structure on the transport behaviors, the identical reconstructed porous electrode is applied in the simulation of cathode and anode as shown in Fig. 10(a). Fig. 10(b) plots the comparative concentration contours of Fe(III) ions in the cathode and V(II) ions in the anode with the porosity of 0.9 and

fibre diameter of 6  $\mu\text{m}$ . It is observed that the similar ion concentration distributions are presented in the cathode and anode. The reason is mainly caused by the same flow condition of catholyte and anolyte. Due to the identical viscosity and porous structure are adopted in this modeling, the flow volumes of ethaline electrolyte in the cathode and anode are equal at the same dimensionless differential pressure. Meanwhile, the consumption rate of reactant is constant under the galvanostatic discharging condition. As a result, the concentration distributions of Fe(III) and V(II) ions as reactant are similar in the cathode and anode at the same flow volume and consumption rate. The differences in diffusivity and reaction constant between the catholyte and anolyte have no influence on the depletion rate of ions during discharging.

Moreover, the comparison of average SOCs in the cathode and anode with different porosity is conducted utilizing this LBM simulation. As shown in Fig. 11(a), the outcome shows that the difference of average SOCs in the catholyte and anolyte is not obvious with varying porosity. That is due to the SOCs are determined by the Fe(III) and V(II) ions concentration in the catholyte and anolyte respectively, according to Eq. (12). The similar concentration distributions of reactant ions lead to the equal SOCs under a given required pumping power and the galvanostatic discharging condition. By contrast, the activation overpotentials in the cathode and anode present an obvious difference as shown in Fig. 11(b). In the identical morphology of porous electrode and flow condition, the absolute value of activation overpotential in the



(a)



(b)

**Fig. 8.** Effect of pore size distribution the local transfer current density of vanadium-iron RFB. (a) Average value of product between local transfer current density and dimensionless specific surface area in porous electrodes with different fibre diameter ( $\epsilon = 0.9$ ); (b) Pore size distribution of porous electrodes with different fibre diameter( $\epsilon = 0.9$ ).

anode is much larger than that in the cathode. The reason can be explained that the lower diffusivity, charge transfer coefficient and reaction constant of vanadium ions cause the weak electrochemical reaction activity in the anode sufficiently.

#### 4.4. Comparison between DES and aqueous electrolyte

Furthermore, the reactive transfer process of vanadium-iron RFB using DES electrolyte is compared to VRFB with aqueous electrolyte under the galvanostatic discharging. In order to improve comparability of two RFBs, this contrastive LB simulation shares the same

porous electrode structure (0.83–0.9 porosity, 10  $\mu\text{m}$  fibre diameter), the same differential pressure (i.e., required pumping power), the same other operating parameters (i.e., inlet SOC, external current density, and inlet concentration) as listed in Table 5. On the other hand, the reactive and transfer property parameters (i.e., viscosity, diffusivity, reaction constant, transfer coefficient), required by LB simulation for the cathode of VRFB, are listed in Table B.1. Meanwhile, the related property parameters of anode of VRFB are given in Table 6.

Using this LB model, the effect of porosity on average SOC in the cathode and anode of VRFB can be calculated as shown in Fig. 12(a). The numerical result shows that the average SOC of VRFB is obviously higher than the vanadium-iron RFB in both cathode and anode. The higher SOC in electrode of VRFB is mainly attributed to the aqueous electrolyte of lower viscosity, which yields a higher flow velocity in the porous electrode at the same differential pressure condition. As discussed above, the depletion time of reactant is shortened with the increasing electrolyte flow velocity, and therefore leads to a higher average SOC. In comparison, a lower flow velocity is presented in the electrodes of vanadium-iron RFB with larger viscosity DES electrolyte, and the variation of SOC affected by porosity is more apparent under the same pumping power condition.

However, although the SOC approaching 0.5 is beneficial to reduce the overpotential of RFB [32], the activation overpotential of VRFB in the cathode is higher than that of vanadium-iron RFB as seen from Fig. 12(b). This could be caused by the reaction constant of vanadium ions in aqueous electrolyte is lower than iron ions in DES electrolyte, thus reducing the reaction activity of redox species. On the contrary, the activation overpotential of VRFB in the anode is lower than that of vanadium-iron RFB. It is noted that the same redox species( $\text{V}^{2+}/\text{V}^{3+}$ ) are used in the anode of two RFBs. Nevertheless, the reactive and transfer properties of vanadium ions display the significant difference in aqueous and DES electrolytes, which can be found in Tables 1 and 6. The poor diffusivity and transfer coefficient of vanadium ions lead to a highest activation overpotential in the anode of vanadium-iron RFB using DES electrolyte. The higher overpotential severely hampers the electrolyte utilization efficiency under the galvanostatic discharging. As an improvement, the overpotential can be reduced using a porous electrode with lower porosity and smaller fibre diameter. As shown in Fig. 12(b), the overpotential in anode decreases by 15.9% when the porosity of porous electrode decreases from 0.9 to 0.83.

## 5. Conclusions

A pore-scale study is performed for understanding the reactive transfer process in the reproducing porous electrodes of vanadium-iron RFB using DES electrolyte. Due to the scarce experimental data about the key property parameters of vanadium-iron RFB with ethaline DES electrolyte, cyclic voltammetry experiment is used to determine the electrochemical and transfer properties of the iron and vanadium ions in ethaline DES electrolyte. A validated pore-scale MRT-LBM is introduced to simulate the electrolyte flow, mass and charge transfer processes coupling with the electrochemical reaction in the cathode and anode of carbon paper which are regenerated utilizing a random reproducing algorithm. Based on the cyclic voltammetry experiment and LBM model, the influences of porous electrode morphology and DES electrolyte transfer properties on the performance of vanadium-iron RFB are elaborated under galvanostatic discharging condition.

The numerical results show that the flow velocity of electrolyte plays an important role in the operation of vanadium-iron RFB under the equal required pumping power. The regenerated carbon paper electrodes with the lower porosity and smaller fibre

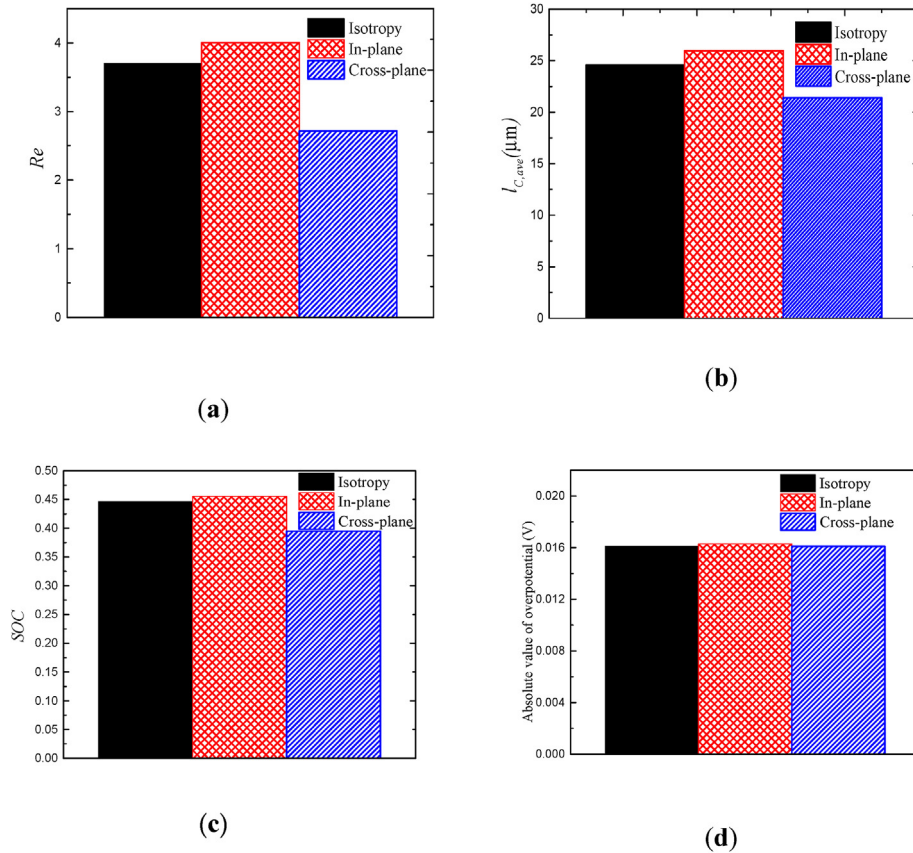


**Fig. 9.** Effect of electrode anisotropy on the performance of vanadium-iron RFB with DES electrolyte. (a) Effect of anisotropy on the electrolyte  $Re$  number; (b) Effect of anisotropy on the mean chord-length; (c) Effect of anisotropy on the average SOC; (d) Effect of anisotropy on the overpotential.

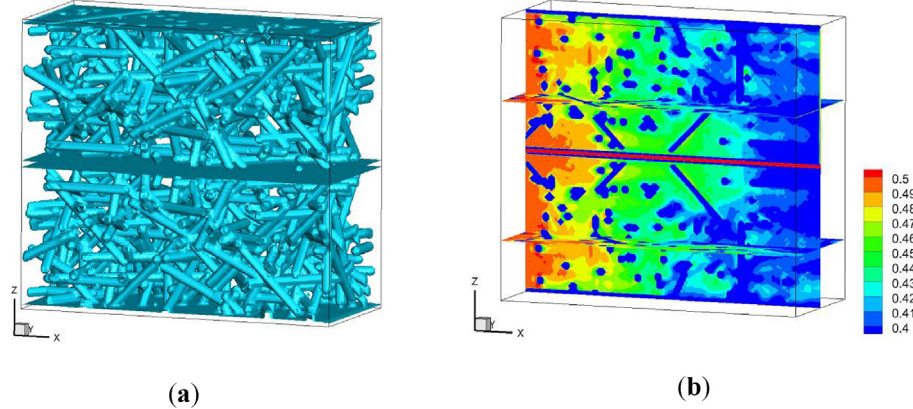
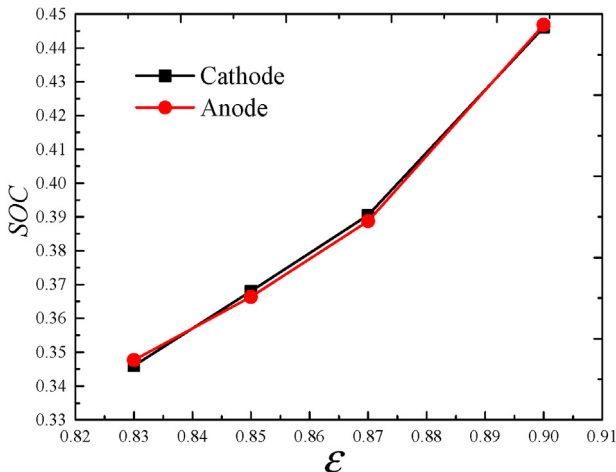


**Fig. 10.** Comparative investigation of reactive transfer process in positive and negative electrode. (a) Schematic diagram of porous electrode; (b) Ions concentration contours in the cathode and anode.

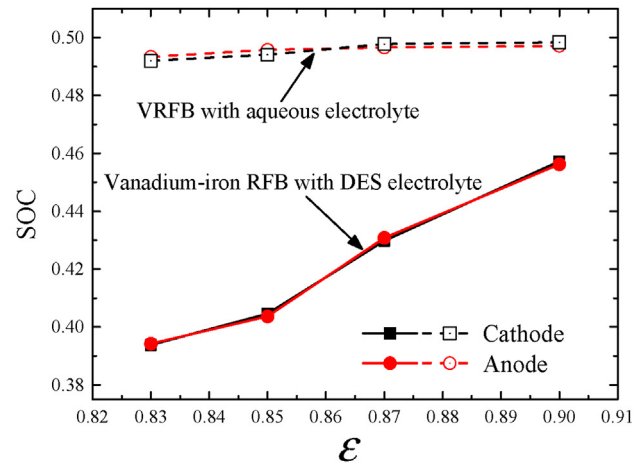
diameter will reduce the permeability of porous electrodes. As a result, the depletion time of reactant is prolonged to lead a lower average SOC of electrolyte in the porous electrodes under the galvanostatic discharging and a given pumping power condition. On the other hand, the regenerated carbon paper electrodes with the higher porosity and larger fibre diameter give rise to the decline of discharging voltage and electrolyte utilization efficiency under the galvanostatic discharging. Meanwhile, at a given porosity, the larger fibre diameter yields the more widespread pore size distribution, resulting in the more apparent non-uniformity of local

current density into the porous electrode. The anisotropy of porous electrode will affect the reactive transfer process due to the difference of permeability in the different pore structures. The electrolyte average flow velocity in the cross-plane porous electrode is lower than that in the isotropic and in-plane porous electrodes, which causes the more depletion of reactants and the lower average SOC in the porous electrode at the same operating conditions.

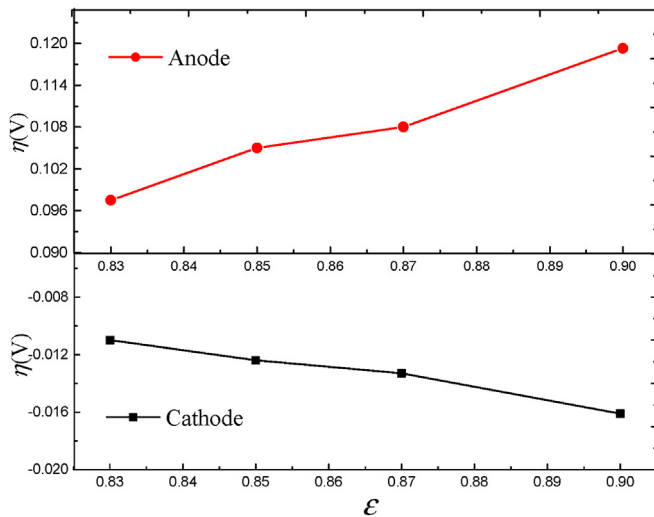
Furthermore, the comparison of operation between the cathode and anode is conducted utilizing this LBM simulation. Due to the



(a)

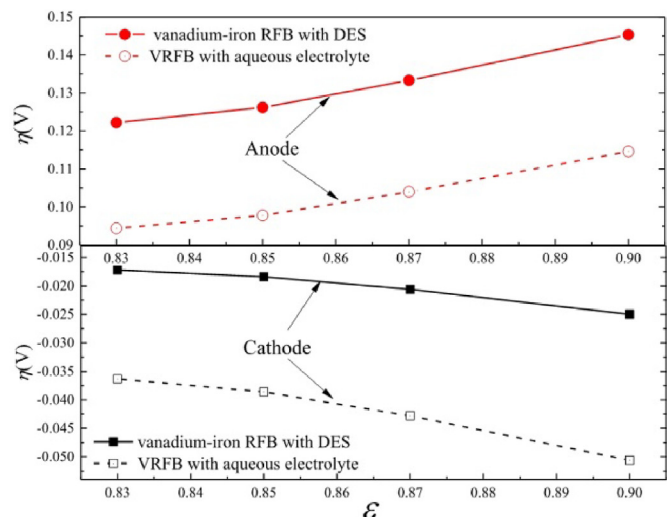


(a)



(b)

**Fig. 11.** Comparative investigation between performance of cathode and anode. (a) Average SOC of electrolyte in the cathode and anode; (b) Overpotential in the cathode and anode.



(b)

**Fig. 12.** Comparative investigation between vanadium-iron RFB with DES electrolyte and VRFB with aqueous electrolyte (Solid lines: vanadium-iron RFB with DES electrolyte; Dash lines: VRFB with aqueous electrolyte). (a) Comparison of average SOC in the cathode and anode; (b) Comparison of overpotential in the cathode and anode.

**Table 6**  
Property parameters of anode of VRFB [19].

Quantity	Value
Reaction constant $k_{0,2}$	$0.17 \times 10^{-6} \text{ m s}^{-1}$
Transfer coefficient $\alpha_2$	0.5
Diffusivity of $V^{2+}$	$2.4 \times 10^{-10} \text{ m}^2 \text{ s}^{-1}$
Diffusivity of $V^{3+}$	$2.4 \times 10^{-10} \text{ m}^2 \text{ s}^{-1}$
Viscosity of electrolyte, $\eta_v$	4.93 mPa s

same flow condition in the catholyte and anolyte, the results show the similar SOC in the cathode and anode. By contrast, the absolute value of overpotential in the anode is much higher than that in the cathode obviously. Moreover, the comparison investigation between vanadium-iron RFB using DES electrolyte and VRFB with aqueous electrolyte shows that the average SOC of VRFB is obviously higher than the vanadium-iron RFB with DES electrolyte under the same pumping power condition, owing to the aqueous electrolyte of lower viscosity. On the other hand, this study reveals

that the cathode of vanadium-iron RFB has the lower activation overpotential comparing with VRFB. On the contrary, the anode of vanadium-iron RFB has highest activation overpotential instead, due to the lower diffusivity and transfer coefficient of vanadium ions in DES electrolyte.

#### Declaration of competing interest

The authors declare that they have no known competing financial interests or personal relationships that could have appeared to influence the work reported in this paper.

#### CRediT authorship contribution statement

**Qiang Ma:** Conceptualization, Funding acquisition, Software, Writing - original draft. **Lijuan Zhao:** Software, Writing - original draft. **Juncai Xu:** Formal analysis, Software. **Huaneng Su:** Resources, Investigation. **Weiqi Zhang:** Resources, Investigation. **Weiwei Yang:** Methodology, Formal analysis. **Qian Xu:** Conceptualization, Funding acquisition, Project administration, Writing - review & editing, Supervision.

#### Acknowledgments

The authors gratefully acknowledge the supports provided by National Natural Science Foundation of China (Grant No.51806083 and No.51676092), China Postdoctoral Science Foundation (Grant No.2018M632242), High-tech Research Key laboratory of Zhenjiang (SS2018002), Natural Science Foundation of Jiangxi Province (20192BAB216027), and a Project Funded by the Priority Academic Program Development of Jiangsu Higher Education Institutions (PAPD), China.

#### Appendix A. A calculation method of the diffusivities in quasi-reversible system

Based on the electrochemical principle [41], the difference between the half-peak potential  $E_{p/2}$  and peak potential  $E_p$  of cyclic voltammetry data in quasi-reversible system can be determined using :

$$E_{p/2} - E_p = \Delta(\lambda, \alpha) \left( \frac{RT}{F} \right) \quad (\text{A.1})$$

where the parameter  $\Delta(\lambda, \alpha)$  also depends on the charge transfer coefficient  $\alpha$  and parameter  $\lambda$ . Using the half-peak potential and the peak potential from cyclic voltammetry measurements, the parameter  $\Delta(\lambda, \alpha)$  can be calculated under the different scan rates. Based on the existing relation curves between  $\lambda$  and  $\Delta$  as  $\alpha = 0.4$  and  $0.5$  [41], the variation of unknown  $\lambda$  with  $\Delta$  as  $\alpha$  ranging from  $0.4$  to  $0.5$  can be estimated by the linear difference method, thereby obtaining the value of  $\lambda$  when  $\alpha = 0.45$  and  $0.49$  as shown in Fig. A.1(a). Then, from  $\lambda$  and  $\alpha$  now, the characteristic parameter  $K(\lambda, \alpha)$  under the different scan rates can be determined using the existing relation curves from literature [41], as shown in Fig. A.1(b). At last, the range of diffusivity of quasi-reversible system can be calculated using the modified Randles-Sevcik equation with the estimated  $K(\lambda, \alpha)$  and the peak current from cyclic voltammetry measurements. Using this calculation method, the ranges of diffusivities in quasi-reversible system are from  $1.08 \times 10^{-11} \text{ m}^2 \text{ s}^{-1}$  to  $1.70 \times 10^{-11} \text{ m}^2 \text{ s}^{-1}$  for iron ions, and from  $1.72 \times 10^{-12} \text{ m}^2 \text{ s}^{-1}$  to  $2.61 \times 10^{-12} \text{ m}^2 \text{ s}^{-1}$  for vanadium ions, respectively.

#### Appendix B. Verification case

In this work, a verification case of VRFB with aqueous electrolyte proposed by You et al. [19] is used to prove the usability of adopted LBM model in the pore-scale simulation of RFB operation. The electrode structure in this verification simulation is simplified as a regular pin electrode as shown in Fig. B.1(a). The LBM model is utilized to predict the overpotentials and voltage drops of this idealized electrode structure as the cathode during the charging process of VRFB. The numerical details were elaborated in existing literature [32,37], and the key simulation parameters are listed in Table B.1.

**Table B.1**  
Operating parameters of verification case [19].

Quantity	Value
Porosity $\epsilon$	0.929
Specific surface area $S$	$16200 \text{ m}^{-1}$
Half-cell width $W$	$0.003 \text{ m}$
External current density $I_{\text{ext}}$	$400 \text{ A m}^{-2}$
Operating temperature, $T$	298 K
Solid Electrical conductivity $\kappa_s$	$1000 \text{ S m}^{-1}$
Reaction constant $k_{0,1}$	$0.68 \times 10^{-6} \text{ m s}^{-1}$
Transfer coefficient $a_1$	0.5
Universal gas constant, $R$	$8.314 \text{ J mol}^{-1} \cdot \text{K}^{-1}$
Diffusivity of $\text{VO}_2^{+/\text{V}^{2+}}$	$3.9 \times 10^{-10} \text{ m}^2 \text{ s}^{-1}$
Diffusivity of $\text{VO}_2^+$	$3.9 \times 10^{-10} \text{ m}^2 \text{ s}^{-1}$
Viscosity of electrolyte, $\eta_v$	$4.93 \text{ mPa s}$
Inlet concentration $C_0$	$1500 \text{ mol m}^{-3}$
Initial proton concentration	$6000 \text{ mol m}^{-3}$
Equilibrium potential, $E_p^0$	1.004 V

Fig.B.1(b) shows the variation of overpotential with different SOCs. It can be found that the overpotential rises sharply when the SOC close to 0% and 100%. The result means the charging efficiency of RFB is suppressed at higher or lower SOC of electrolyte. Under the joint contributions of effective voltage and overpotential, the nonlinear relationship between cell voltage and SOC is presented as shown in Fig. B.1 (c). The verification case demonstrates that the prediction from this LBM model is in agreement with the research result of other literature.

#### Appendix C. Reproducing detail of 3D porous electrode

The details of this generation algorithm are as follows: (1) A random core node is generated based on a core distribution probability. (2) A random numbers pair(within 0-2π) is assigned to two azimuth angles for determining 3D fiber orientation of isotropic porous structure. (3) Based on the selected core node and two azimuth angles, a line extending to the boundaries is generated in the reconstruction domain. (4) Using this line as the axis of the cylinder, a fibre with fixed radius can be obtained. Then, other carbon fibres are generated by repeating steps 1–4, and the reproducing procedure is terminated when the desired fibre fraction is achieved. Using the above reproducing algorithm, the isotropic fibre porous structures can be generated with the desired porosity ( $\epsilon$ ) and the fibre diameter ( $d_f$ ), as shown in Fig. C.1(a)-(c).

In addition, this random generation method also can be built the anisotropic porous structures through controlling the distribution probability of azimuth angles. If the value of azimuth angle  $\beta$  is fixed to 0 or  $\pi$ (along x-axis direction in this procedure), and other azimuth angle is assigned as a random number(within 0-2π), the anisotropic porous structure is generated as shown in Fig.C.1(d). By contrast, if the value of azimuth angle  $\beta$  is fixed to  $\pi/2$  or  $3\pi/2$ (alone z-axis direction in this procedure), the anisotropic porous structure is generated as shown in Fig. C.1 (e).

## Appendix D. Supplementary data

Supplementary data to this article can be found online at  
<https://doi.org/10.1016/j.electacta.2020.136486>.

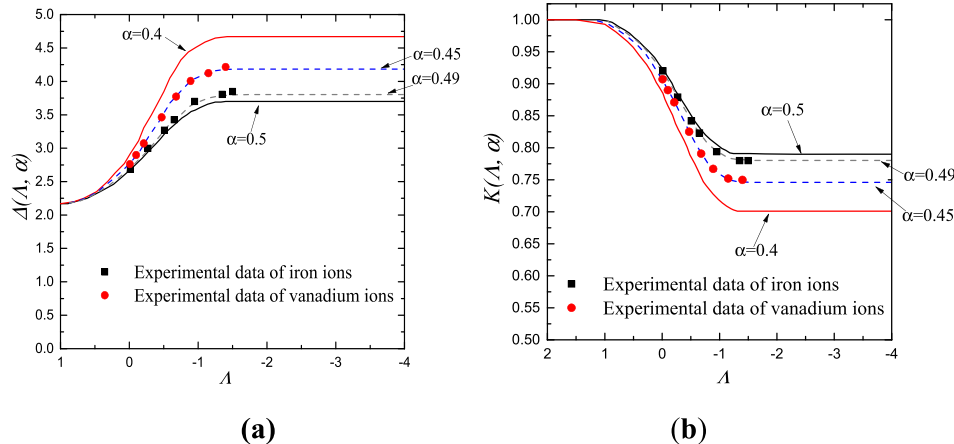


**Fig. A.1.** Dependence of characteristic parameters on the  $A$  and  $\alpha$ . (a)  $D(A, \alpha)$ ; (b)  $K(A, \alpha)$ .

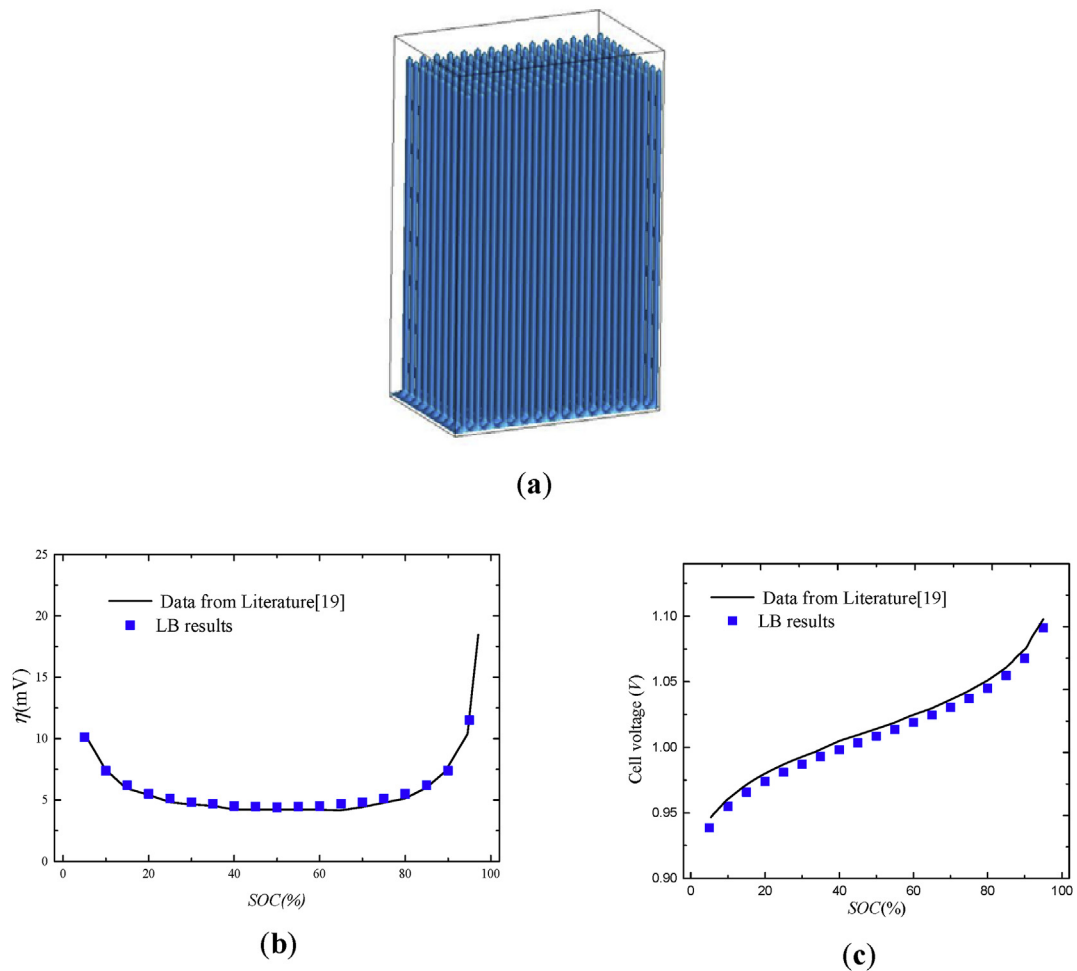


**Fig. B.1.** Verification case of VRFB with aqueous electrolyte. (a) Schematic diagram of regular pin electrode; (b) Variation of overpotential with different SOC; (c) Variation of cell voltage with different SOC.

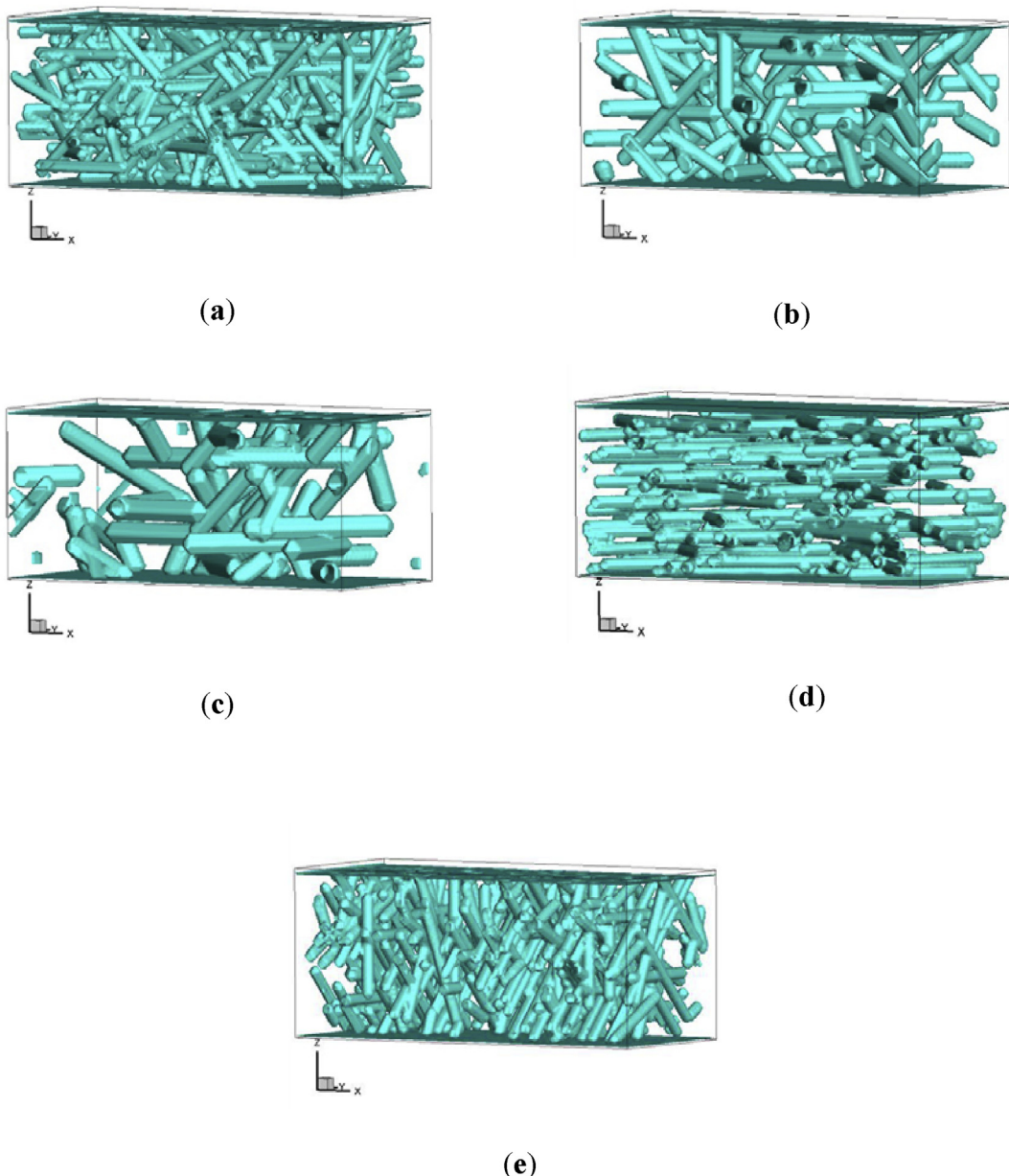


**Fig. C.1.** 3D model geometries of generated porous structures. (a) Isotropy,  $\epsilon = 0.9$ ,  $d_f = 6 \mu\text{m}$ ; (b) Isotropy,  $\epsilon = 0.9$ ,  $d_f = 10 \mu\text{m}$ ; (c) Isotropy,  $\epsilon = 0.9$ ,  $d_f = 14 \mu\text{m}$ ; (d) In-plane,  $\epsilon = 0.9$ ,  $d_f = 6 \mu\text{m}$ ; (e) Cross-plane,  $\epsilon = 0.9$ ,  $d_f = 6 \mu\text{m}$ .

## References

- [1] G. Cong, Y.C. Lu, Organic eutectic electrolytes for future flow batteries, *Chem* 4 (2018) 2732.
- [2] B.W. Zhang, Y. Lei, B.F. Bai, T.S. Zhao, A two-dimensional model for the design of flow fields in vanadium redox flow batteries, *Int. J. Heat Mass Tran.* 135 (2019) 460.
- [3] C. Mostert, B. Ostrander, S. Bringezu, T. Kneiske, Comparing electrical energy storage technologies regarding their material and carbon footprint, *Energies* 11 (2018) 3386.
- [4] P.K. Leung, A.A. Shah, L. Sanz, C. Flox, J.R. Morante, Q. Xu, M.R. Mohamed, C. Ponce-deLeon, F.C. Walsh, Recent developments in organic redox flow batteries : a critical review, *J. Power Sources* 360 (2017) 243.
- [5] J. Shen, S. Liu, Z. He, L. Shi, Influence of antimony ions in negative electrolyte on the electrochemical performance of vanadium redox flow batteries, *Electrochim. Acta* 151 (2015) 297.
- [6] C. Zhang, L. Zhang, Y. Ding, X. Guo, G. Yu, Eutectic electrolytes for high-energy-density redox flow batteries, *ACS Energy Lett* 3 (2018) 2875.
- [7] A.P. Abbott, G. Capper, D.L. Davies, R.K. Rasheed, V. Tambyrajah, Novel solvent properties of choline chloride/urea mixtures, *Chem. Commun.* (2003) 70.
- [8] Q. Zhang, K. De Oliveira Vigier, S. Royer, F. Jerome, Deep eutectic solvents: syntheses, properties and applications, *Chem. Soc. Rev.* 41 (2012) 7108.
- [9] H. Chen, Y.-C. Lu, A high-energy-density multiple redox semi-solid-liquid flow battery, *Adv. Energy Mater.* 6 (2016) 1502183.
- [10] D. Lloyd, T. Vainikka, K. Kontturi, The development of an all copper hybrid redox flow battery using deep eutectic solvents, *Electrochim. Acta* 100 (2013) 18.
- [11] D. Lloyd, T. Vainikka, M. Ronkainen, K. Kontturi, Characterisation and application of the Fe(II)/Fe(III) redox reaction in an ionic liquid analogue, *Electrochim. Acta* 109 (2013) 843.
- [12] Q. Xu, T.S. Zhao, L. Wei, C. Zhang, X.L. Zhou, Electrochemical characteristics and transport properties of Fe(II)/Fe(III) redox couple in a non-aqueous reline deep eutectic solvent, *Electrochim. Acta* 154 (2015) 462.
- [13] Q. Xu, L. Qin, H. Su, L. Xu, P. Leung, C. Yang, H. Li, Electrochemical and transport characteristics of V(II)/V(III) redox couple in a nonaqueous deep eutectic solvent: temperature effect, *J. Energy Eng.* 143 (2017), 04017051.
- [14] Q. Xu, L.Y. Qin, Y.N. Ji, P.K. Leung, H.N. Su, F. Qiao, W.W. Yang, A.A. Shah, H.M. Li, A deep eutectic solvent (DES) electrolyte-based vanadium-iron redox

- flow battery enabling higher specific capacity and improved thermal stability, *Electrochim. Acta* 293 (2019) 426.
- [15] Q. Xu, Y.N. Ji, L.Y. Qin, P.K. Leung, F. Qiao, Y.S. Li, H.N. Su, Evaluation of redox flow batteries goes beyond round-trip efficiency: A technical review, *J. Energy Storage* 16 (2018) 108.
- [16] K. Lin, R. Gamez-Bombarelli, E.S. Beh, L. Tong, Q. Chen, A. Valle, A.n. Aspuru-Guzik, M.J. Aziz, R.G. Gordon, A redox-flow battery with an alloxazine-based organic electrolyte, *Nat. Energy* 1 (2016) 16102.
- [17] Q. Xu, T.S. Zhao, Fundamental models for flow batteries, *Prog. Energy Combust. Sci.* 49 (2015) 40.
- [18] A.A. Shah, M.J. Watt-Smith, F.C. Walsh, A dynamic performance model for redox-flow batteries involving soluble species, *Electrochim. Acta* 53 (2008) 8087.
- [19] D. You, H. Zhang, J. Chen, A simple model for the vanadium redox battery, *Electrochim. Acta* 54 (2009), 6827–683.
- [20] D. You, H. Zhang, J. Chen, Theoretical analysis of the effects of operational and designed parameters on the performance of a flow-through porous electrode, *J. Electroanal. Chem.* 625 (2009) 165.
- [21] K. Yaji, S. Yamasaki, S. Tushima, T. Suzuki, K. Fujita, Topology optimization for the design of flow fields in a redox flow battery, *Struct. Multidiscip. Optim.* 57 (2017) 535.
- [22] L. Chen, Y.L. Feng, C.X. Song, L. Chen, Y.L. He, W.Q. Tao, Multi-scale modeling of proton exchange membrane fuel cell by coupling finite volume method and lattice Boltzmann method, *Int. J. Heat Mass Tran.* 63 (2013) 268.
- [23] L. Chen, Q. Kang, Q. Tang, B.A. Robinson, Y.-L. He, W.-Q. Tao, Pore-scale simulation of multicomponent multiphase reactive transport with dissolution and precipitation, *Int. J. Heat Mass Tran.* 85 (2015) 935.
- [24] F. Wu, Z. Rao, The lattice Boltzmann investigation of natural convection for nanofluid based battery thermal management, *Appl. Therm. Eng.* 115 (2017) 659.
- [25] H. Liang, H.H. Liu, Z.H. Chai, B.C. Shi, Lattice Boltzmann method for contact-line motion of binary fluids with high density ratio, *Phys. Rev. E* 99 (2019), 063306.
- [26] Z. Liu, H. Wu, Pore-scale modeling of immiscible two-phase flow in complex porous media, *Appl. Therm. Eng.* 93 (2016) 1394.
- [27] H. Xu, Z. Dang, Lattice Boltzmann modeling of carbon deposition in porous anode of a solid oxide fuel cell with internal reforming, *Appl. Energy* 178 (2016) 294.
- [28] Z. Chai, C. Huang, B. Shi, Z. Guo, A comparative study on the lattice Boltzmann models for predicting effective diffusivity of porous media, *Int. J. Heat Mass Tran.* 98 (2016) 687.
- [29] Z.Y. Jiang, Z.G. Qu, L. Zhou, W.Q. Tao, A microscopic investigation of ion and electron transport in lithium-ion battery porous electrodes using the lattice Boltzmann method, *Appl. Energy* 194 (2017) 530.
- [30] Z.Y. Jiang, Z.G. Qu, L. Zhou, Lattice Boltzmann simulation of ion and electron transport during the discharge process in a randomly reconstructed porous electrode of a lithium-ion battery, *Int. J. Heat Mass Tran.* 123 (2018) 500.
- [31] M.D.R. Kok, R. Jervis, T.G. Tranter, M.A. Sadeghi, D.J.L. Brett, P.R. Shearing, J.T. Gostick, Mass transfer in fibrous media with varying anisotropy for flow battery electrodes: direct numerical simulations with 3D X-ray computed tomography, *Chem. Eng. Sci.* 196 (2019) 104.
- [32] G. Qiu, A.S. Joshi, C.R. Dennison, K.W. Knehr, E.C. Kumbur, Y. Sun, 3-D pore-scale resolved model for coupled species/charge/fluid transport in a vanadium redox flow battery, *Electrochim. Acta* 64 (2012) 46.
- [33] G. Qiu, C.R. Dennison, K.W. Knehr, E.C. Kumbur, Y. Sun, Pore-scale analysis of effects of electrode morphology and electrolyte flow conditions on performance of vanadium redox flow batteries, *J. Power Sources* 219 (2012) 223.
- [34] L. Chen, Y.L. He, W.Q. Tao, P. Zelenay, R. Mukundan, Q. Kang, Pore-scale study of multiphase reactive transport in fibrous electrodes of vanadium redox flow batteries, *Electrochim. Acta* 248 (2017) 425.
- [35] D. Zhang, Q. Cai, O.O. Taiwo, V. Yufit, N.P. Brandon, S. Gu, The effect of wetting area in carbon paper electrode on the performance of vanadium redox flow batteries: a three-dimensional lattice Boltzmann study, *Electrochim. Acta* 283 (2018) 1806.
- [36] D. Zhang, A. Forner-Cuenca, O.O. Taiwo, V. Yufit, F.R. Brushett, N.P. Brandon, S. Gu, Q. Cai, Understanding the role of the porous electrode microstructure in redox flow battery performance using an experimentally validated 3D pore-scale lattice Boltzmann model, *J. Power Sources* 447 (2020) 227249.
- [37] Q. Ma, Q. Xu, Q. Chen, Z. Chen, H. Su, W. Zhang, Lattice Boltzmann model for complex transfer behaviors in porous electrode of all copper redox flow battery with deep eutectic solvent electrolyte, *Appl. Therm. Eng.* 160 (2019) 114015.
- [38] C. Flox, J. Rubio-Garcia, R. Nafria, R. Zamani, M. Skoumal, T. Andreu, J. Arbiol, A. Cabot, J.R. Morante, Active nano-cupt3 electrocatalyst supported on graphene for enhancing reactions at the cathode in all-vanadium redox flow batteries, *Carbon* 50 (6) (2012) 2372.
- [39] X. Wei, W. Xu, M. Vijayakumar, L. Cosimescu, T. Liu, V. Sprengle, W. Wang, Tempo-based catholyte for high-energy density nonaqueous redox flow batteries, *Adv. Mater.* 26 (45) (2014) 7649.
- [40] J. Xu, Q. Ma, H. Su, F. Qiao, P. Leung, A.A. Shah, Q. Xu, Redox characteristics of iron ions in different deep eutectic solvents, *Ionics* 26 (2020) 483.
- [41] A.J. Bard, L.R. Faulkner, *Electrochemical Methods: Fundamentals and Applications (Chemistry)*, John Wiley & Sons, New York, 2001.
- [42] R.S. Nicholson, Theory and application of cyclic voltammetry for measurement of electrode reaction kinetics, *Anal. Chem.* 37 (1965) 1351.
- [43] S.H. Lee, H.Y. Fang, W.C. Chen, Electrochemical characterization of screen-printed carbon electrodes by modification with chitosan oligomers, *Electroanalysis* 17 (23) (2005) 2170.
- [44] Q. Kang, P.C. Lichtner, D. Zhang, An improved lattice Boltzmann model for multicomponent reactive transport in porous media at the pore scale, *Water Resour. Res.* 43 (12) (2007) W12S14.
- [45] H.R. Jiang, Y.K. Zeng, M.C. Wu, W. Shyy, T.S. Zhao, A uniformly distributed bismuth nanoparticle-modified carbon cloth electrode for vanadium redox flow batteries, *Appl. Energy* 240 (2019) 226.
- [46] T. Liu, X. Li, H. Nie, C. Xu, H. Zhang, Investigation on the effect of catalyst on the electrochemical performance of carbon felt and graphite felt for vanadium flow batteries, *J. Power Sources* 286 (2015) 73.
- [47] L. Yu, F. Lin, W. Xiao, L. Xu, J. Xi, Achieving efficient and inexpensive vanadium flow battery by combining  $\text{Ce}(\text{Zr}_{1-x}\text{O}_2)$  electrocatalyst and hydrocarbon membrane, *Chem. Eng. J.* 356 (2019) 622.
- [48] H. Zhang, N. Chen, C. Sun, X. Luo, Investigations on physicochemical properties and electrochemical performance of graphite felt and carbon felt for iron-chromium redox flow battery, *Int. J. Energy Res.* 44 (2020) 3839.
- [49] M. Wang, Q. Kang, N. Pan, Thermal conductivity enhancement of carbon fiber composites, *Appl. Therm. Eng.* 29 (2019) 418.
- [50] D. Zhang, Q. Cai, S. Gu, Three-dimensional lattice-Boltzmann model for liquid water transport and oxygen diffusion in cathode of polymer electrolyte membrane fuel cell with electrochemical reaction, *Electrochim. Acta* 262 (2018) 282–296.
- [51] D. Lloyd, T. Vainikka, L. Murtomäki, K. Kontturi, E. Ahlberg, The kinetics of the  $\text{Cu}^{2+}/\text{Cu}^+$  redox couple in deep eutectic solvent, *Electrochim. Acta* 56 (14) (2011) 4942.
- [52] B.R. Gebart, Permeability of unidirectional reinforcements for RTM, *J. Compos. Mater.* 26 (8) (1992) 1100.
- [53] S. Torquato, B. Lu, Chord-length distribution function for two-phase random media, *Phys. Rev. E* 47 (4) (1993) 2950–2953.
- [54] J. Comiti, M. Renaud, A new model for determining mean structure parameters of fixed beds from pressure drops measurements: application to beds packed with parallelepipedal particles, *Chem. Eng. Sci.* 44 (9) (1989) 1539–1545.